

Hybrid SAR Speckle Reduction Using Complex Wavelet Shrinkage and Non-Local PCA-Based Filtering

Ramin Farhadiani, Saeid Homayouni, *Senior Member, IEEE*, and Abdolreza Safari,

In this paper, a new hybrid despeckling method, based on Undecimated Dual-Tree Complex Wavelet Transform (UDT-CWT) using *maximum a posteriori* (MAP) estimator and non-local Principal Component Analysis (PCA)-based filtering with local pixel grouping (LPG-PCA), was proposed. To achieve a heterogeneous-adaptive speckle reduction, SAR image is classified into three classes of point targets, details, or homogeneous areas. The despeckling is done for each pixel based on its class of information. Logarithm transform was applied to the SAR image to convert the multiplicative speckle into additive noise. Our proposed method contains two principal steps. In the first step, denoising was done in the complex wavelet domain via MAP estimator. After performing UDT-CWT, the noise-free complex wavelet coefficients of the log-transformed SAR image were modeled as a two-state Gaussian mixture model. Furthermore, the additive noise in the complex wavelet domain was considered as a zero-mean Gaussian distribution. In the second step, after applying inverse UDT-CWT, an iterative LPG-PCA method was used to smooth the homogeneous areas and enhance the details. The proposed method was compared with some state-of-the-art despeckling methods. The experimental results showed that the proposed method leads to a better speckle reduction in homogeneous areas while preserving details.

Index Terms—Gaussian mixture model, homomorphic transformation, non-local filtering, undecimated dual-tree complex wavelet transform.

I. INTRODUCTION

Synthetic Aperture Radar (SAR) images are inherently affected by a signal-dependent granular noise-like phenomenon called speckle, which is the nature of all coherent systems. The presence of speckle in the SAR images decreases the performance of various pattern recognition applications such as classification, change detection, and biomass estimation. Hence, a primary preprocessing step, namely despeckling, is needed to suppress the speckle phenomena.

As yet, various spatial domain filters have been proposed in the literature for reducing the speckle in SAR images; among others, Lee [1], Frost [2], and Kuan [3] are the most popular and frequently used filters. Although these methods have a decent ability to smooth flat areas, they suffer from many problems.

For example, they are sensitive to the size and shape of the used kernel.

Multi-Resolution Analysis (MRA) method, introduced in the early 1990s, can overcome the before mentioned disadvantages of spatial filters. Wavelet transform, with all its variation and further developments, has been extensively used for denoising images that corrupted with Additive White Gaussian Noise (AWGN) and speckle. However, speckle in SAR images has multiplicative nature and should be converted to an additive one. For this propose, the first solution is using the logarithm transform (homomorphic filtering) and the second one is conducted by rewriting the observed signal as a sum of signal and signal dependent noise (non-homomorphic filtering) [4]–[6]. However, denoising in the wavelet domain can be done by thresholding the wavelet coefficients or by employing the Bayesian theory. The performance of speckle reduction methods based on Bayesian theory is highly dependent on the appropriate probability distribution function (PDF) that was used as a prior model for describing the noise-free wavelet coefficients. In [7], Mallat described that the distribution of wavelet coefficients is non-Gaussian, symmetric, and sharply peaked around zero with heavy tails. To capture this heavy-tailed property, various PDFs, e.g., Cauchy [8], [9], bivariate Cauchy [10], Gaussian mixture [11], [12], and Laplace mixture [13], [14] PDFs within the MAP, MMSE, and MMAE estimators in the Wavelet, Dual-Tree Complex Wavelet, Contourlet, Directionlet, and Lapped Domains have been used in the literature. However, these methods may have some limitations, such as presented ringing effect near edges or isolated patterns in homogeneous areas, which make the despeckling results visually annoying.

Recently, with the advent of non-local means filtering (NLM) [15] for reducing the additive Gaussian noise, this idea was extended to suppress the speckle from SAR images [16]–[25], as well as Polarimetric SAR image despeckling [26], [27]. Besides these non-local despeckling approaches, some despeckling methods based on neural networks [28]–[30] and total variation [31], [32] were also presented in the literature.

As mentioned in [33], a suitable SAR speckle reduction method must satisfy the following characteristics: 1) reduce speckle in homogeneous areas; 2) preserve details of SAR image such as edges, texture, point targets, and urban areas; 3) radiometric preservation; and 4) artifact-free. In this article, we proposed a novel hybrid heterogeneous-adaptive speckle reduction method based on complex wavelet shrinkage and non-local Principal Component Analysis (PCA)-based filtering. Since the classic wavelet transform has some limitations and suffers from several fundamental shortcomings such as the lack of shift invariance and poor directional selectivity [34], we utilized the Undecimated Dual-Tree Complex Wavelet Transform (UDT-CWT) [35] that is shift invariant and isolate edges with different orientations in different subbands. Also, we used non-local PCA-based denoising with local pixel grouping (LPG-PCA) [36] in our proposed method. First, by some predefined kernels, three classes of heterogeneity, e.g., point targets, details (contain lines and edges), or homogeneous areas are extracted from the SAR image. After that, our proposed method starts with two principal

59 steps. In the first step, despeckling was done in the complex wavelet domain within *maximum a posteriori* (MAP)
 60 estimator. In the second step, by employing an iterative LPG-PCA method, the flat areas were completely smoothed, and
 61 the details were enhanced.

62 II. PROPOSED DESPECKLING METHOD

63 If S is theoretically noise-free SAR image (or reflectivity) and η is fully developed speckle, then the model of observed
 64 SAR image I can be expressed as $I = S \cdot \eta$ [33]. From this equation, we can find that speckle is multiplicative
 65 phenomenon in nature. To convert this multiplicative noise into an additive one, we can take a logarithm transform from
 66 both sides of this equation and we have

$$67 \quad Z = X + N \quad (1)$$

68 where Z , X , and N are the logarithm transform of I , S and η , respectively. In the next subsections, we describe how to
 69 classify the SAR image into various classes of heterogeneity, and explain how to use these classes to better suppress the
 70 speckle from a SAR image.

71 A. Classification Strategy

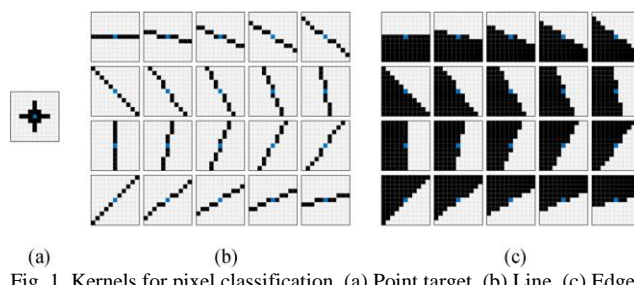
72 To achieve a heterogeneous-adaptive speckle reduction, many methods have been proposed in the literature [4]–[6],
 73 [12], [14], [20], [23]. In this article, we used the ratio detector to classify SAR image. In this method, each pixel was
 74 classified into three classes of heterogeneity such as point targets, details, or homogeneous areas. To this end, we proposed
 75 to use common ratio detectors [37]. The kernels that are used to identify the point targets, lines, and edges are shown in
 76 Fig. 1. To decrease the computational cost, we used predefined fixed-size 11×11 kernels. The ratio detector to point
 77 targets detection can be computed as $R_{pt} = R_2 / R_1$ where R_1 and R_2 represent the average of values in dark and white
 78 pixels in the defined kernel, respectively. If R_{pt} is smaller (or equal) than the threshold T_{pt} , the pixel will be assigned as
 79 point target. In the case of edges and lines detection, the ratio detector can be defined as

$$80 \quad R_{e-l} = \begin{cases} R_1/R_2 & \text{if } R_1/R_2 \leq 1 \\ R_2/R_1 & \text{if } R_2/R_1 \leq 1 \end{cases} \quad (2)$$

81 After computing R_{e-l} for each direction, the minimum value of R_{e-l} will be considered as the direction of the interested
 82 pixel. It should be noted that the different kernels were used to identify the lines (Fig. 1b) and the edges (Fig. 1c). After
 83 that, the edges and lines maps will be fused together to achieve fusion map as

$$84 \quad \text{map}_f = \sqrt{(\text{map}_e^2 + \text{map}_l^2)} / 2 \quad (3)$$

85 where map_e , map_l , and map_f represent the edges, lines, and fused maps, respectively. In the last stage, the map_f has to
 86 be normalized between $[0, 1]$. The final details map can be computed as $\text{map}_f < T_d$, where T_d is a threshold. It should
 87 be noted that choosing a small T_{pt} or T_d can cause fewer point targets and details detection, respectively. While larger
 88 thresholds can find more pixels as point targets and details. For this reason, T_{pt} and T_d should be chosen based on the
 89 content of the SAR image. To achieve better classification result, we performed a light low-pass Gaussian filter on the
 90 SAR image before applying the classification strategy. Also, to remove the false detected details, especially in the case
 91 of single-look SAR image, by employing a local 3×3 window, we will remove the neighbors that contain details fewer
 92 than 4 pixels. Fig. 2 shows a single-look real SAR data named Toronto. Moreover, this figure represents point targets and
 93 details maps. After classifying the SAR image into three classes, the speckle suppression is done based on each class
 94 information. To save the point targets, they will be completely excluded from the despeckling process and, at the end,
 95 they will be back to their original locations.



105 Fig. 1. Kernels for pixel classification. (a) Point target. (b) Line. (c) Edge.
 106

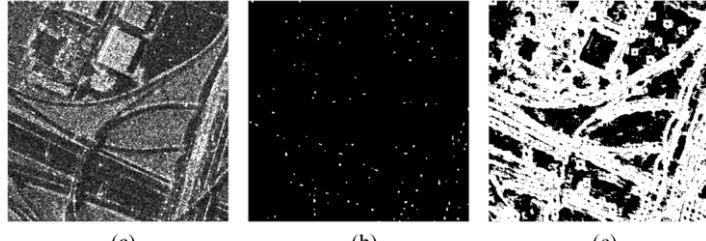


Fig. 2. Classification result. (a) Real SAR image. (b) Point targets map. (c) Final details map.

110 B. Step 1

111 In this step, the homogeneous areas were despeckled in the complex wavelet domain, and also a light despeckling was
 112 performed on the detected details. In (1), we assume that the signal and noise components are independent random
 113 variables and N is considered as an additive noise. Because the UDT-CWT is a linear transformation, after applying it to
 114 (1) to up to scale j , the noisy complex wavelet coefficients y at each scale can be written as $y_j^i = w_j^i + n_j^i$ where w and n
 115 are the noise-free coefficients and the noise component, respectively. Also, subscript i denotes the orientations
 116 $\pm 15^\circ, \pm 45^\circ, \pm 75^\circ$. For the sake of clarity, we omitted j and i . Our goal here is to estimate w from the noisy observation
 117 y . For this purpose, we used the MAP estimator. The Bayesian MAP estimator can be written as

$$118 \quad \hat{w}(y) = \arg \max_{\hat{w}} [p_n(y - n)p_w(w)] \quad (4)$$

120 where $p_n(y - n)$ and $p_w(w)$ are the noise component and the noise-free complex wavelet coefficients, respectively. In
 121 the proposed method, the noise component in the complex wavelet domain assumed to be zero mean Gaussian PDF with
 122 the standard deviation σ_n . By considering this assumption, if $p_w(w)$ is assumed to be a zero-mean Gaussian density with
 123 standard deviation σ_n , then the estimator can be written as $\hat{w}(y) = (\sigma^2/\sigma^2 + \sigma_n^2) \cdot y$ [38]. In this equation, σ_n is unknown
 124 and it can be estimated by a robust median estimator from subband HH in the first and second scales of the complex
 125 wavelet coefficients as $\hat{\sigma}_n = (D_1 + D_2)/2$ [39], where D_i can be computed as $D_i = \text{median}(|HH_i|)/0.6745, i = 1, 2$
 126 [40]. As mentioned before, a proper speckle reduction filtering has to flat the homogeneous areas while preserving the
 127 image features and their corresponding spatial information. To this end, an additional parameter, namely smoothing factor
 128 (C), is multiplied into $\hat{\sigma}_n$. Here, we introduce two types of C factors: C_h for homogeneous class and C_d for details class.
 129 These two parameters have to be tuned according to the content of the image. In low signal-to-noise ratio images, e.g.,
 130 single-look SAR image, C_h might have a large value. However, if C_h is too large, the image will be over-smoothed. In
 131 contrast, by increasing the number of looks, speckle in the SAR image decreases. Hence, we can choose a lower value
 132 for C_h . Based on our experiments, for the homogeneous class, the C_h is in the range between one and three. However, for
 133 details class, C_d must be chosen below one, in order to preserve the details and perform light noise reduction on them.

134 In this paper, we will employ a two-state Gaussian mixture PDF for modeling $p_w(w)$ as

$$137 \quad p_w(w) = \alpha_1 p_1(w) + \alpha_2 p_2(w) = \alpha_1 \cdot \frac{1}{\sigma_1^2 \sqrt{2}} \exp\left(-\frac{w^2}{2\sigma_1^2}\right) + \alpha_2 \cdot \frac{1}{\sigma_2^2 \sqrt{2}} \exp\left(-\frac{w^2}{2\sigma_2^2}\right) \quad (5)$$

138 where σ_1 and σ_2 denote the standard deviation of Gaussian components 1 and 2, respectively, whereas α_1 and α_2 represent
 139 their corresponding weights. In (5), σ_1 , σ_2 , α_1 and α_2 are unknown and should be estimated. For this purpose, we will use
 140 the iterative local Expectation-Maximization algorithm as described in [12]. Computing the unknown parameters locally
 141 can increase the performance of the despeckling. If the window size is too big, the estimated parameters were closed to
 142 their global value. Based on our experimental results, we used a fixed-size 15×15 neighborhood for computing the
 143 parameters of the Gaussian mixture PDF. Because we use mixture PDF, we must use the averaged version of the MAP
 144 estimator (AMAP) [41] to estimate \hat{w} from y . The AMAP estimator can be expressed as

$$145 \quad \hat{w}(y) = \frac{\sum_{i=1}^2 \alpha_i p_i \hat{w}_i}{\sum_{i=1}^2 \alpha_i p_i} \quad (6)$$

146 In the case of Gaussian noise, \hat{w} is equal to $\hat{w}_i = (\sigma_i^2/\sigma_i^2 + \sigma_n^2) \cdot y, i = 1, 2$. Because y is the sum of w and independent
 147 Gaussian noise, the PDF of y is the convolution of two independent Gaussian PDFs with variance σ_i^2 and σ_n^2 , respectively.
 148 Therefore, p_i is a Gaussian PDF with variance $\sigma_i^2 + \sigma_n^2$ as $1/\sqrt{2\pi(\sigma_i^2 + \sigma_n^2)} \exp(-y^2/2(\sigma_i^2 + \sigma_n^2))$. Substituting \hat{w}_i and
 149 p_i into (6) yields the following estimator:

$$150 \quad \hat{w}(y) = \frac{\left(\sum_{i=1}^2 \alpha_i \exp\left(-y^2/2(\sigma_n^2 + \sigma_i^2)\right) \sigma_i^2 \right) / \sqrt{2\pi(\sigma_n^2 + \sigma_i^2)^3}}{\left(\sum_{i=1}^2 \alpha_i \exp\left(-y^2/2(\sigma_n^2 + \sigma_i^2)\right) \right) / \sqrt{2\pi(\sigma_n^2 + \sigma_i^2)}} \cdot y \quad (7)$$

157 After denoising the all complex wavelet coefficients based on (7), the inverse UDT-CWT is applied.
 158
 159

C. Step 2

160 After despeckling the SAR image in the complex wavelet domain, we proposed to use the LPG-PCA method developed
 161 in [36]. Using the LPG-PCA method can efficiently decrease the undesired artifact that may appear in the homogeneous
 162 areas, as well as enhance the details. In this subsection, we will briefly describe the LPG-PCA method. For more details,
 163 we refer the readers to [36]. Since the remaining noise after taking inverse UDT-CWT is still additive in the log-
 164 transformed domain, by considering (1), the noise N and the noise-free data X assumed uncorrelated. Hence, the
 165 covariance matrix of Z can be calculated as $\Sigma_Z = \Sigma_X + \Sigma_N$, where Σ_N is equivalent to the noise variance (σ^2). The variance
 166 of the log-transformed speckle can be computed as $\psi(1, L)$ and $0.25 \times \psi(1, L)$ in the intensity and square root intensity
 167 SAR images, respectively, where L represents the number of looks and $\psi(1, L)$ denotes the first-order Polygamma function
 168 of L [42]. In this article, L is computed using an unsupervised method proposed in [43]. Like the smoothing factor defined
 169 in previous subsection, for reaching the better denoising result, we will multiply σ^2 into a positive constant θ . Similar to
 170 the smoothing factor, θ can control the level of noise reduction in the second step of the proposed algorithm. A large θ
 171 causes over-smoothing, while a small θ may not be able to reduce the noise in the SAR image. Based on our experiments,
 172 this parameter could be chosen above 1. In the LPG-PCA method, for a given pixel to be denoised, we considered an M
 173 $\times M$ variable block centered on it in which contains all the components within the window, and denoted by $= [z_1, \dots, z_m]^T$
 174 , $m = M^2$. In a variable block, we have $z = x + n$, where $x = [x_1, \dots, x_m]^T$, $n = [n_1, \dots, n_m]^T$. To calculating the
 175 PCA in order to estimate the x , we considered an $S \times S$ ($S > M$) training block around desired pixel. Here, we used a $41 \times$
 176 41 training block, as well as a 7×7 variable block. In this method, selecting and grouping the training samples that are
 177 similar to the central $M \times M$ block is done based on block matching method. The matrix that contains the grouped patches
 178 can be written as $Z = [z^1, z^2, \dots, z^n]$, where $z^k, k = 1, \dots, n$ and $n = (S - M + 1)^2$ is the k th column vector of Z . In
 179 the next step, we should centralize the Z (e.g., \bar{Z}) as $\bar{z}^k = z^k - E(z^k)$, where $E(\cdot)$ represents the expectation operation.
 180 After that, the PCA transform is applied on \bar{Z} and we have $\Sigma_{\bar{Z}} = P \Lambda_{\bar{Z}} P^T$, where $\Sigma_{\bar{Z}}$, P , and $\Lambda_{\bar{Z}}$ denote the covariance
 181 matrix of the \bar{Z} , eigenvector, and diagonal eigenvalue matrixes, respectively. By applying P to the \bar{Z} , we have $\bar{Y}_N = P^T \bar{Z}$.
 182 Now, the Linear Minimum Mean Square Error (LMMSE) criterion is employed to reduce the noise component in \bar{Y}_N and
 183 obtain \hat{Y} matrix. Finally, by reverse PCA transform and adding the mean values back, \hat{X} is obtained.
 184 Actually, most of the noise were removed in step 1 and step 2. However, we can iterate step 2 one more time to achieve
 185 a better denoising result. It should be noted that in the next iteration, σ^2 must be updated as
 186

$$\sigma_{iter+1}^2 = \left| \sigma_{iter}^2 - E[(\hat{X}_{iter} - \hat{X}_{iter-1})^2] \right|$$

187 where σ_{iter+1}^2 is the variance of log-transformed speckle in the next iteration, \hat{X}_{iter-1} is the estimated log-transformed SAR
 188 image in the previous iteration, and $E[\cdot]$ denotes the expectation. It should be noticed here that to prevent the over-
 189 smoothing, we multiplied θ into σ^2 only in the first iteration. A block diagram of our proposed despeckling algorithm is
 190 also shown in Fig. 3. It should be noted that due to the use of the logarithmic transformation, the mean of the log-
 191 transformed speckle field is biased [44] and it is not equal to zero. Therefore, this biased mean should be corrected by
 192 subtracting the mean value of the log-transformed speckle from the output image of “step 2.”
 193

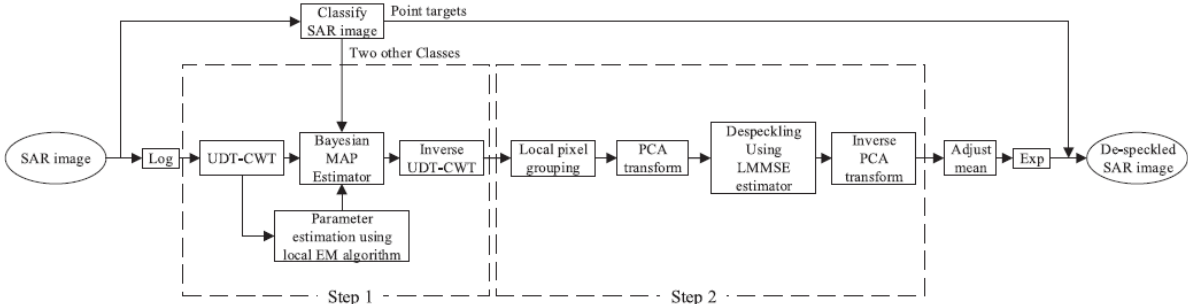


Fig. 3. The workflow of the proposed despeckling method.

III. EXPERIMENTAL RESULTS

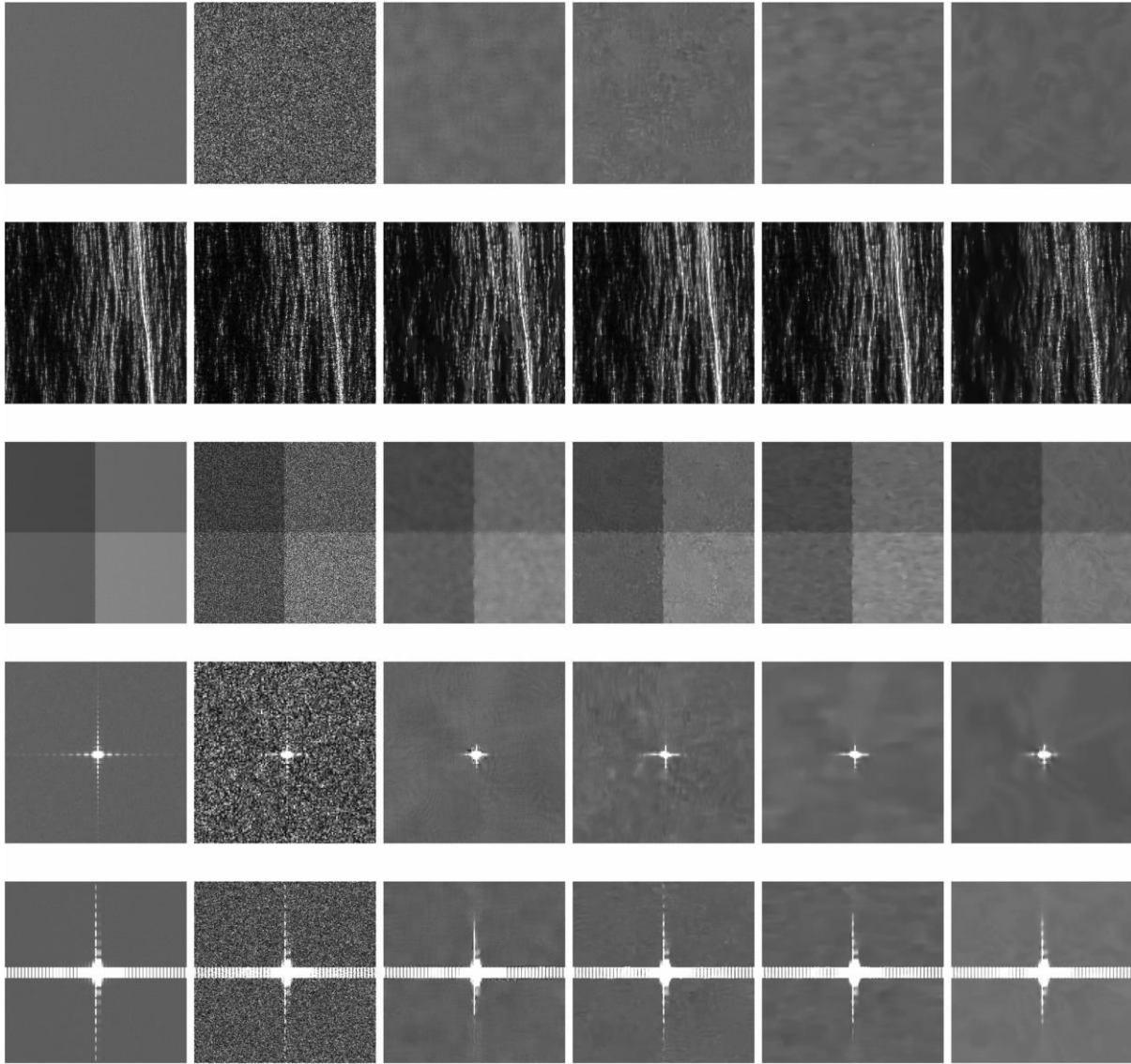
194 This section presents the results of the performance analysis of the proposed speckle reduction method based on
 195 benchmarking data developed in [45] and two real SAR images (TerraSAR-X from Toronto, and AIRSAR over San
 196 Francisco). For comparison, we used several state-of-the-art despeckling methods. The first one is the iterative
 197 Probabilistic Patch-Based (PPB) [16] despeckling method. The iterative PPB method uses $\alpha = 0.92$, $T = 0.2$, 21×21
 198 search window with a patch size of 7×7 and 25 iterations. Moreover, the SARBM3D [17] and FANS [18] despeckling
 199 methods were employed. The source codes of the PPB, SARBM3D, and FANS methods are available at [46], [47], and
 200 [48], respectively. For the proposed algorithm, four levels of complex wavelet decomposition were considered. Also, T_{pt}
 201 and T_d were equal to 0.25 and 0.65, for benchmarking datasets, as well as 0.5 and 0.78 for Toronto image and 0.5 and
 202 0.85 for San Francisco image, respectively. Furthermore, C_h , C_d , and θ are considered as 0.3, 1, and 1.5 for benchmarking
 203

208 datasets; in addition, these parameters are equal to 0.1, 3, and 1.8 for Toronto image, as well as 0.1, 1, and 1.3 for San
209 Francisco image, respectively.

210

211 A. Performance Evaluation Using Benchmarking Data

212 The benchmarking datasets used in this subsection were available at [49]. In this article, we only used some objective
213 indicators proposed in [45] for single-look simulated Homogeneous, Digital Elevation Model (DEM), Squares, Corner,
214 and Building reference datasets and we do not discuss how these datasets were generated or how to compute these
215 indicators. For this reason, we refer the readers to [45] for more information. The refined version of Equivalent Number
216 of Looks, referred as ENL*, was considered for Homogeneous image to evaluate the speckle suppression in homogeneous
217 areas. The coefficient of variation (C_x) and Despeckling Gain (DG) were used for measuring the texture preservation and
218 SNR improvement for DEM image. Figure of Merit (FOM) is employed as edge-preserving measuring indicator for
219 Squares image. The contrast values C_{NN} and C_{BG} are used for evaluating the radiometric preservation through the filtering
220 process in Corner image. C_{DR} and Building Smearing (BS), which respectively measure the radiometric precision and
221 distortion of radiometric building profile in the range direction, were used for Building image. In the ideal case, the
222 computed values for ENL*, DG, and FOM should be a large value; also, computed values for C_x , C_{NN} , C_{BG} , C_{DR} , and
223 BS should be close to their clean values. As pointed out in [45], the goal of using these measuring datasets is not to find
224 which method is better than others or which is the best one; nevertheless, it is to gain an insight about the ability and
225 limitations of despeckling methods. Table I demonstrates the computed indicators for the PPB, SARBM3D, FANS, and
226 the proposed method. All the results reported in Table I were obtained by averaging the despeckling results over eight
227 independent single-look images of the same scene. Also, Fig. 4 represents clean, noisy, and despeckled images of each
228 dataset. In Homogeneous image, our proposed method showed its ability to smooth flat areas. By the visual inspection,
229 we can find that all methods generated some artifacts, especially in the SARBM3D and FANS outputs. In the DEM image,
230 SARBM3D gained the nearest value to clean C_x ; also the best value for DG indicator was obtained by SARBM3D over
231 5 dB, followed by the FANS method. In the case of edge preserving, the PPB and SARBM3D methods have similar
232 results and were the best. However, appearance of artifacts in flat areas is not deniable in all methods, especially in
233 the SARBM3D and FANS results. In the case of corner reflector, the best strategy is to avoid perform any filtering on the
234 detected corner reflector. By investigating the C_{NN} and C_{BG} values, we can find that our proposed method follows this
235 strategy, as shown in Fig 4. Also, the SARBM3D and FANS methods provide acceptable results, except the PPB method
236 which has lower C_{NN} and C_{BG} values. At the end, by investigating the C_{DR} and BS values, we can find that our proposed
237 method has good performance to preserved building features.



244
245 Fig. 4. From top to bottom, Homogeneous, DEM (256×256 zoomed area), Squares, Corner (128×128 zoomed area), and Building images,
246 respectively. From left to right, clean, noisy, PPB, SARBM3D, FANS, and proposed method despeckling results, respectively.
247
248
249

TABLE I
PERFORMANCE COMPARISON ON THE BENCHMARKING DATASETS

		Clean	PPB	SARBM3D	FANS	Proposed
Hom.	ENL*	510.36	141.01	111.91	161.15	339.90
DEM	Cx	2.40	2.71	2.43	2.55	2.85
	DG	Inf	3.68	5.32	4.99	3.64
Squ.	FOM	0.926	0.819	0.818	0.799	0.797
Cor.	CNN	7.75	3.71	7.39	7.05	7.75
	CBG	36.56	32.70	35.45	35.37	37.14
Build.	CDR	65.90	64.90	65.91	65.66	64.44
	BS	0.00	3.13	1.46	3.51	0.58

250
251
252 **B. Performance Evaluation Using Real SAR Data**

253 The two real SAR images used in this subsection for performance evaluation are TerraSAR-X image of Toronto,
254 Canada, 1-meter resolution, and AIRSAR L-band from San Francisco, USA, 10-meter resolution. These SAR datasets
255 are in amplitude format for HH and VV polarization, respectively. The number of looks (L) of these datasets is considered
256 to be about one and four for Toronto and San Francisco images, respectively. These datasets are presented in Fig. 5. To
257 make a quantitative comparison, some numerical non-referenced indexes were used in this subsection, including
258 Equivalent Number of Looks (ENL), Edge-Preservation Degree based on Ratio of Average (EPD-ROA), and Mean of
259 Ratio image (Mor). The ENL is widely used to evaluate the speckle suppression in homogeneous areas. For the SAR
260 image in amplitude format, the ENL can be computed as $(4/\pi - 1) \times (\mu/\sigma)^2$ [44], where μ and σ are mean and standard
261 deviation values computed from a homogeneous area. The higher value of ENL represents the much speckle suppression.
262 The EPD-ROA indicator can be computed as [50]

263

264

265

266 where I_{S1} and I_{S2} represent the adjacent pixel values of the despeckled image along horizontal or vertical direction,
 267 whereas I_{I1} and I_{I2} denote the corresponding adjacent pixel values of speckled image, respectively. In the ideal case, the
 268 EPD-ROA index is close to one and its value closer to one shows better edge preservation ability. The MoR between the
 269 SAR image before and after despeckling indicates the capability of the despeckling method for radiometric preservation,
 270 and in the ideal case, it should be equal to one. The results of despeckling of these two datasets are shown in Fig. 5. Also,
 271 Table II shows the computed values for various despeckling methods, regarding ENL and EPD-ROA in both horizontal
 272 and vertical directions and MoR. Among all despeckling methods, our proposed method achieves the better results, in
 273 terms of speckle reduction in homogeneous areas, while preserving the point targets and details. Also, Fig. 6 represents
 274 the zoomed area of Toronto image. By visual comparison of these figures, we can find that the SARBM3D method can
 275 preserve the details at the expense of poor speckle reduction in flat areas. The performance of the FANS method is better
 276 than the SARBM3D method, but it is still not the best. As the PPB method has effective speckle suppression and details
 277 preserving, it smoothed out some point targets, due to using a non-local approach, as can be seen from Fig. 6. Based on
 278 this figure, we observe that the proposed method has the best point targets preserving, while at the same time, the
 279 homogeneous areas are smooth and details are preserved. Also, with the analysis of MoR values, we can say that our
 280 proposed method has good ability to avoid radiometric distortion. As a result, we can say that our proposed method has
 281 a worthy performance in speckle suppression in homogeneous areas, while it preserves the point targets and details.

282 To evaluate the computational complexity of the despeckling methods, all the despeckling codes were executed on a
 283 PC with Intel Core i3-3220 CPU, 3.30 GHz, and 8 GB RAM. Also, the Toronto image (320×320) is employed for
 284 execution time comparison. The execution time of the methods was approximately around 108, 35, 4, and 92 s for the
 285 PPB, SARBM3D, FANS, and the proposed method, respectively. The FANS method have the fastest execution time, due
 286 to using variable-size search area, as well as probabilistic early termination approach and employing look-up tables.
 287 Although the PPB and the proposed method use non-local approach, their execution time is acceptable. However, the
 288 SARBM3D method is faster than the PPB and the proposed method. It should be noted that the proposed algorithm can
 289 achieve a better tradeoff between speckle reduction in homogeneous areas while preserving details and performing no-
 290 filtering on the point targets among others.

291



292

293

294

295



Fig. 5. Results obtained from real SAR images (first row, Toronto ($L=1$) and second row, San Francisco ($L=4$)). From left to right, real SAR image, PPB, SARBM3D, FANS, and proposed method despeckling results, respectively.

296

297

298

299

300

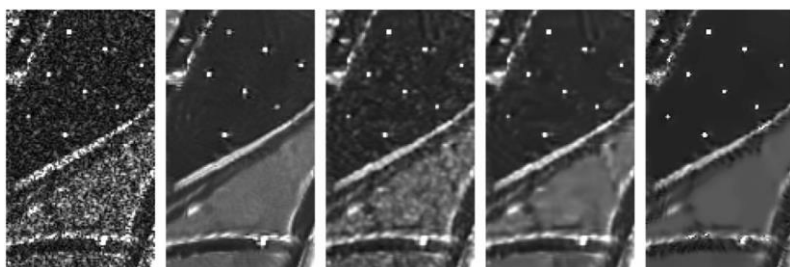


Fig. 6. The zoomed area images. From left to right, real SAR image, PPB, SARBM3D, FANS, and proposed method, respectively.

TABLE II
ENL, EPD-ROA, AND MOR VALUES

Results with Toronto

Despeckling Methods	ENL		EPD-ROA		MoR
	Zone 2	Zone 1	H	V	
PPB	30.933	19.148	0.6693	0.6858	0.863
SAR-BM3D	6.375	5.534	0.6726	0.6893	0.873
FANS	20.166	15.175	0.6640	0.6816	0.856
Proposed	45.894	47.842	0.6775	0.6948	0.995
Results with San Francisco					
Despeckling Methods	ENL		EPD-ROA		MoR
	Zone 2	Zone 1	H	V	
PPB	111.224	73.959	0.9441	0.9368	0.959
SAR-BM3D	24.008	13.514	0.9457	0.9311	0.955
FANS	73.507	27.970	0.9359	0.9171	0.952
Proposed	239.617	291.722	0.9617	0.9473	0.964

301

302

303

IV. CONCLUSION

304

305

306

307

308

309

310

311

312

313

314

315

316

317

318

319

320

321

322

323

324

325

326

327

328

329

330

331

332

333

334

335

336

337

338

339

340

341

342

343

344

345

346

347

348

349

350

351

352

This paper proposed a hybrid speckle reduction method for SAR images. The idea in this article was to combine the complex wavelet shrinkage and non-local filtering. Also, to achieve a heterogeneous-adaptive despeckling, a classification stage was added to the algorithm. Experimental results showed that the proposed method provides both effective speckle reduction in homogeneous areas and details preservation altogether. However, due to using UDT-CWT and non-local approach, our proposed method is relatively time-consuming. Furthermore, a few parameters in our method have to be optimally tuned to achieve the best results, which will be the subject of further research works on advanced optimization approaches.

ACKNOWLEDGMENT

REFERENCES

- [1] J.-S. Lee, "Speckle suppression and analysis for synthetic aperture radar images," *Opt. Eng.*, vol. 25, no. 5, pp. 636–643, 1986.
- [2] V. S. Frost, J. A. Stiles, K. S. Shanmugan, and J. C. Holtzman, "A model for radar images and its application to adaptive digital filtering of multiplicative noise," *IEEE Trans. Pattern Anal. Mach. Intell.*, vol. PAMI-4, no. 2, pp. 157–166, Mar. 1982.
- [3] D. T. Kuan, A. A. Sawchuk, T. C. Strand, and P. Chavel, "Adaptive noise smoothing filter for images with signal-dependent noise," *IEEE Trans. Pattern Anal. Mach. Intell.*, vol. PAMI-7, no. 2, pp. 165–177, Mar. 1985.
- [4] T. Bianchi, F. Argenti, and L. Alparone, "Segmentation-based map despeckling of SAR images in the undecimated wavelet domain," *IEEE Trans. Geosci. Remote Sens.*, vol. 46, no. 9, pp. 2728–2742, Sep. 2008.
- [5] F. Argenti, T. Bianchi, A. Lapini, and L. Alparone, "Fast map despeckling based on Laplacian–Gaussian modeling of wavelet coefficients," *IEEE Geosci. Remote Sens. Lett.*, vol. 9, no. 1, pp. 13–17, Jan. 2012.
- [6] H.-C. Li, W. Hong, Y.-R. Wu, and P.-Z. Fan, "Bayesian wavelet shrinkage with heterogeneity-adaptive threshold for SAR image despeckling based on generalized gamma distribution," *IEEE Trans. Geosci. Remote Sens.*, vol. 51, no. 4, pp. 2388–2402, Apr. 2013.
- [7] S. Mallat, "A theory for multiresolution signal decomposition: The wavelet representation," *IEEE Trans. Pattern Anal. Mach. Intell.*, vol. 11, no. 7, pp. 674–693, Jul. 1989.
- [8] M. I. H. Bhuiyan, M. O. Ahmad, and M. Swamy, "Spatially adaptive wavelet-based method using the cauchy prior for denoising the SAR images," *IEEE Trans. Circuits Syst. Video Technol.*, vol. 17, no. 4, pp. 500–507, Apr. 2007.
- [9] Q. Gao, Y. Lu, D. Sun, Z.-L. Sun, and D. Zhang, "Directionlet-based denoising of SAR images using a Cauchy model," *Signal Process.*, vol. 93, no. 5, pp. 1056–1063, 2013.
- [10] J. J. Ranjani and S. Thiruvengadam, "Dual-tree complex wavelet transform based SAR despeckling using interscale dependence," *IEEE Trans. Geosci. Remote Sens.*, vol. 48, no. 6, pp. 2723–2731, Jun. 2010.
- [11] Y. Lu, Q. Gao, D. Sun, and D. Zhang, "Directionlet-based method using the Gaussian mixture prior to SAR image despeckling," *Int. J. Remote Sens.*, vol. 35, no. 3, pp. 1143–1161, 2014.
- [12] D. Hazarika, V. K. Nath, and M. Bhuyan, "SAR image despeckling based on a mixture of Gaussian distributions with local parameters and multiscale edge detection in lapped transform domain," *Sens. Imag.*, vol. 17, no. 1, p. 15, 2016.
- [13] Y. Lu, Q. Gao, D. Sun, Y. Xia, and D. Zhang, "SAR speckle reduction using Laplace mixture model and spatial mutual information in the directionlet domain," *Neurocomputing*, vol. 173, pp. 633–644, 2016.
- [14] D. Hazarika, V. Nath, and M. Bhuyan, "SAR image despeckling based on combination of Laplace mixture distribution with local parameters and multiscale edge detection in lapped transform domain," *Procedia Comput. Sci.*, vol. 87, pp. 140–147, 2016.

- [15] A. Buades, B. Coll, and J.-M. Morel, "A non-local algorithm for image denoising," in *Proc. IEEE Conf. Comput. Vis. Pattern Recog.*, vol. 2, 2005, pp. 60–65.
- [16] C. A. Deledalle, L. Denis, and F. Tupin, "Iterative weighted maximumlikelihood denoising with probabilistic patch-based weights," *IEEE Trans. Image Process.*, vol. 18, no. 12, pp. 2661–2672, Dec. 2009.
- [17] S. Parrilli, M. Poderico, C. V. Angelino, and L. Verdoliva, "A nonlocal SAR image denoising algorithm based on LLMMSE wavelet shrinkage," *IEEE Trans. Geosci. Remote Sens.*, vol. 50, no. 2, pp. 606–616, Feb. 2012.
- [18] D. Cozzolino, S. Parrilli, G. Scarpa, G. Poggi, and L. Verdoliva, "Fast adaptive nonlocal SAR despeckling," *IEEE Trans. Geosci. Remote Sens. Lett.*, vol. 11, no. 2, pp. 524–528, Feb. 2014.
- [19] C. A. Deledalle, L. Denis, F. Tupin, A. Reigber, and M. Jäger, "A unified nonlocal framework for resolution-preserving (pol)(in) SAR denoising," *IEEE Trans. Geosci. Remote Sens.*, vol. 53, no. 4, pp. 2021–2038, Apr. 2015.
- [20] D. Gragnaniello, G. Poggi, G. Scarpa, and L. Verdoliva, "SAR image despeckling by soft classification," *IEEE J. Sel. Topics Appl. Earth Observ. Remote Sens.*, vol. 9, no. 6, pp. 2118–2130, Jun. 2016.
- [21] G. Di Martino, A. Di Simone, A. Iodice, G. Poggi, D. Riccio, and L. Verdoliva, "Scattering-based SARBM3D," *IEEE J. Sel. Topics Appl. Earth Observ. Remote Sens.*, vol. 9, no. 6, pp. 2131–2144, Jun. 2016.
- [22] X. Ma, H. Shen, X. Zhao, and L. Zhang, "SAR image despeckling by the use of variational methods with adaptive nonlocal functionals," *IEEE Trans. Geosci. Remote Sens.*, vol. 54, no. 6, pp. 3421–3435, Jun. 2016.
- [23] F. Liu, J. Wu, L. Li, L. Jiao, H. Hao, and X. Zhang, "A hybrid method of SAR speckle reduction based on geometric-structural block and adaptive neighborhood," *IEEE Trans. Geosci. Remote Sens.*, vol. 56, no. 2, pp. 730–748, Feb. 2018.
- [24] D. Guan, D. Xiang, X. Tang, and G. Kuang, "SAR image despeckling based on nonlocal low-rank regularization," *IEEE Trans. Geosci. Remote Sens.*, pp. 1–18, Dec. 2018.
- [25] Z. Yu, W. Wang, C. Li, W. Liu, and J. Yang, "Speckle noise suppression in SAR images using a three-step algorithm," *Sensors*, vol. 18, no. 11, 2018, Art. no. 3643.
- [26] X. Ma, P. Wu, Y. Wu, and H. Shen, "A review on recent developments in fully polarimetric SAR image despeckling," *IEEE J. Sel. Topics Appl. Earth Observ. Remote Sens.*, vol. 11, no. 3, pp. 743–758, Mar. 2018.
- [27] X. Ma, P. Wu, and H. Shen, "Multifrequency polarimetric SAR image despeckling by iterative nonlocal means based on a space frequency information joint covariance matrix," *IEEE J. Sel. Topics Appl. Earth Observ. Remote Sens.*, vol. 12, no. 1, pp. 274–284, Jan. 2019.
- [28] G. Chierchia, D. Cozzolino, G. Poggi, and L. Verdoliva, "SAR image despeckling through convolutional neural networks," in *Proc. IEEE Int. Geosci. Remote Sens. Symp.*, 2017, pp. 5438–5441.
- [29] P. Wang, H. Zhang, and V. M. Patel, "SAR image despeckling using a convolutional neural network," *IEEE Signal Process. Lett.*, vol. 24, no. 12, pp. 1763–1767, Dec. 2017.
- [30] X. Tang, L. Zhang, and X. Ding, "SAR image despeckling with a multilayer perceptron neural network," *Int. J. Digit. Earth*, vol. 12, pp. 1–21, 2018.
- [31] D.-Q. Chen and L.-Z. Cheng, "Spatially adapted total variation model to remove multiplicative noise," *IEEE Trans. Image Process.*, vol. 21, no. 4, 2012, Art. no. 1650.
- [32] D. Gleich, "Optimal-dual-based l_1 analysis for speckle reduction of SAR data," *IEEE Trans. Geosci. Remote Sens.*, vol. 56, no. 11, pp. 6674–6685, Nov. 2018.
- [33] C. Oliver and S. Quegan, *Understanding Synthetic Aperture Radar Images*. Raleigh, NC, USA: SciTech, 2004.
- [34] I. W. Selesnick, R. G. Baraniuk, and N. C. Kingsbury, "The dual-tree complex wavelet transform," *IEEE Signal Process. Mag.*, vol. 22, no. 6, pp. 123–151, Nov. 2005.
- [35] P. R. Hill, N. Anantrasirichai, A. Achim, M. E. Al-Mualla, and D. R. Bull, "Undecimated dual-tree complex wavelet transforms," *Signal Process. Image Commun.*, vol. 35, pp. 61–70, 2015.
- [36] L. Zhang, W. Dong, D. Zhang, and G. Shi, "Two-stage image denoising by principal component analysis with local pixel grouping," *Pattern Recog.*, vol. 43, no. 4, pp. 1531–1549, 2010.
- [37] A. Lopes, E. Nezry, R. Touzi, and H. Laur, "Structure detection and statistical adaptive speckle filtering in sar images," *Int. J. Remote Sens.*, vol. 13, no. 9, pp. 1735–1758, 1993.
- [38] M. K. Mihcak, I. Kozintsev, K. Ramchandran, and P. Moulin, "Lowcomplexity image denoising based on statistical modeling of wavelet coefficients," *IEEE Signal Process. Lett.*, vol. 6, no. 12, pp. 300–303, Dec. 1999.
- [39] M. I. H. Bhuiyan, M. O. Ahmad, and M. Swamy, "Wavelet-based despeckling of medical ultrasound images with the symmetric normal inverse Gaussian prior," in *Proc. IEEE Int. Conf. Acoust., Speech, Signal Process.*, vol. 1, 2007, pp. 721–724.
- [40] D. L. Donoho, "De-noising by soft-thresholding," *IEEE Trans. Inf. Theory*, vol. 41, no. 3, pp. 613–627, May 1995.
- [41] H. Rabbani and S. Gazor, "Image denoising employing local mixture models in sparse domains," *IET Image Process.*, vol. 4, no. 5, pp. 413–428, Oct. 2010.
- [42] H. Xie, L. E. Pierce, and F. T. Ulaby, "Statistical properties of logarithmically transformed speckle," *IEEE Trans. Geosci. Remote Sens.*, vol. 40, no. 3, pp. 721–727, Mar. 2002.
- [43] Y. Cui, G. Zhou, J. Yang, and Y. Yamaguchi, "Unsupervised estimation of the equivalent number of looks in SAR images," *IEEE Geosci. Remote Sens. Lett.*, vol. 8, no. 4, pp. 710–714, Jul. 2011.
- [44] H. Xie, L. E. Pierce, and F. T. Ulaby, "SAR speckle reduction usingwavelet denoising and Markov random field modeling," *IEEE Trans. Geosci. Remote Sens.*, vol. 40, no. 10, pp. 2196–2212, Oct. 2002.
- [45] G. D. Martino, M. Poderico, G. Poggi, D. Riccio, and L. Verdoliva, "Benchmarking framework for SAR despeckling," *IEEE Trans. Geosci. Remote Sens.*, vol. 52, no. 3, pp. 1596–1615, Mar. 2014.

- 415 [46] Jan. 29, 2019. [Online]. Available: <https://www.charles-deledalle.fr/pages/ppb.php>
416 [47] May 30, 2013. [Online]. Available: <http://www.grip.unina.it/research/80-sar-despeckling/80-sar-bm3d.html>
417 [48] Jul. 30, 2013. [Online]. Available: <http://www.grip.unina.it/research/86-sar-despeckling/86-fans.html>
418 [49] May 21, 2013. [Online]. Available: <http://www.grip.unina.it/research/80-sar-despeckling/85.html>
419 [50] H. Feng, B. Hou, and M. Gong, “SAR image despeckling based on local homogeneous-region segmentation by using
420 pixel-relativity measurement,” *IEEE Trans. Geosci. Remote Sens.*, vol. 49, no. 7, pp. 2724–2737, Jul. 2011.